J. Fluid Mech. (2018), *vol.* 853, *pp.* 601–620.
doi:10.1017/jfm.2018.579

Duelling dry zones around hygroscopic droplets

Saurabh Nath[1], Caitlin E. Bisbano[1], Pengtao Yue[2] and Jonathan B. Boreyko[1,†]

[1]Department of Biomedical Engineering and Mechanics, Virginia Tech, Blacksburg, VA 24061, USA

[2]Department of Mathematics, Virginia Tech, Blacksburg, VA 24061, USA

(Received 22 December 2017; revised 11 July 2018; accepted 20 July 2018; first published online 29 August 2018)

In the 1480s, da Vinci invented the first hygrometer using cellulose fibres to attract moisture from the atmosphere. Five hundred years later, Williams and Blanc showed that the depressed vapour pressure of a hygroscopic sessile droplet can inhibit condensation within an annular dry zone on the surface. What remains unresolved to this day is whether these regions of suppressed condensation around hygroscopic agents are due to inhibited nucleation versus inhibited growth of the condensate. We elucidate the competition between these two mechanisms by generating steady-state dry zones about frozen water droplets. The choice of ice as the hygroscopic material was motivated by its unique ability to remain undiluted as it attracts moisture from the air. Experiments, scaling models, and simulations where the ice droplet size, ambient humidity and surface temperature are systematically varied reveal that over the vast majority of the parameter space, the inhibited growth dry zone wins the duel over the nucleation dry zone.

Key words: condensation/evaporation, drops, icing

1. Introduction

Hygroscopic substances attract water molecules from the surrounding humid air. Under fluctuating environmental conditions, the sorption/desorption cycles of hygroscopic materials have enabled the development of heat pumps (Chan, Ling-Chin & Roskilly 2013), thermal batteries (Narayanan *et al.* 2015) and hygromorphic actuators and engines (Reyssat & Mahadevan 2009; Chen *et al.* 2015) inspired by seed-dispersal mechanisms for pine cones and wheat plants (Dawson, Vincent & Rocca 1997). When a hygroscopic droplet is deposited onto a substrate, its depressed vapour pressure prevents condensation from forming within an annular dry zone on the surface, even under supersaturated conditions (Williams & Blanc 1981). Many follow-up works have utilized salts (Guadarrama-Cetina *et al.* 2014), glycols (Sun *et al.* 2015) or nectars (Biswas *et al.* 2015) to study these dry zones for potential anti-fogging or anti-frosting applications. It is therefore surprising that the physics governing the extent of a dry zone about a hygroscopic agent remain mostly unclear to this day.

Our current lack of understanding is partly due to the inability to obtain steady-state dry zones. Traditional hygroscopic materials necessarily become diluted over time

† Email address for correspondence: boreyko@vt.edu

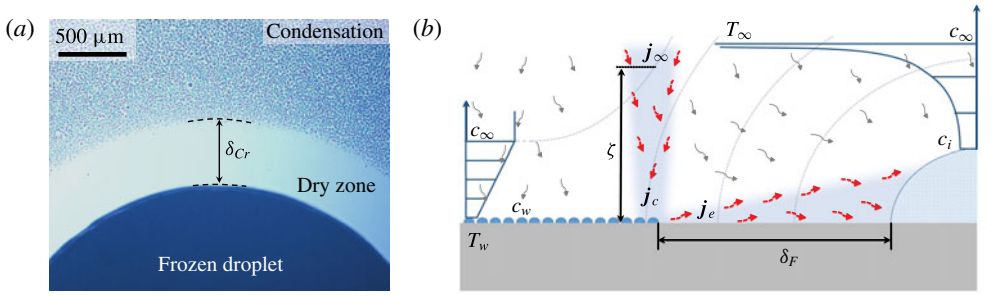

FIGURE 1. (*a*) A micrograph of a frozen water droplet creating a stable dry zone between itself and the surrounding condensation. The frozen droplet has a contact radius of $R = 1.7$ mm, while the liquid condensate beyond the dry zone are of the order $a \sim 1$–10 μm. The surface temperature was $T_w = -10\,^\circ$C and the ambient conditions were $T_\infty = 16\,^\circ$C and $H = 50\,\%$. (*b*) Schematic of the vapour flow about the dry zone. A hyperbolic profile (right side of schematic) defines the vapour concentration extending from the isolated frozen droplet, which will be used to predict the extent of the nucleation dry zone (δ_N). Even once liquid droplets have nucleated, their out-of-plane diffusive growth must at least match their in-plane evaporation due to the ice droplet (bold variables in the middle of the schematic); this balance governs a flux dry zone (δ_F). The concentration boundary layer thickness, ζ, extends from the surface to the ambient vapour concentration. See § 5 for the full details regarding this model.

as they harvest moisture, which leads to the decay and collapse of dry zones (Guadarrama-Cetina *et al.* 2014; Sun *et al.* 2015; Sun & Rykaczewski 2016). For example, a salt crystal deposited on a surface initially provokes a dry zone during condensation, but as the salt becomes hydrated this dry zone collapses within mere seconds (Guadarrama-Cetina *et al.* 2015). A further complication is the possibility of two competing mechanisms for dry zone formation – inhibition of nucleation versus inhibition of growth of condensate. Historically, the formation of dry zones was solely attributed to the inhibition of nucleation (Aizenberg, Black & Whitesides 1999; Guadarrama-Cetina *et al.* 2014; Biswas *et al.* 2015). Here, we will call this type of dry zone a nucleation dry zone (δ_N) for short. However, in 2015 a second mechanism was proposed that posited inhibited growth (Guadarrama-Cetina *et al.* 2015), which we will call a flux dry zone (δ_F). To date, no reports have measured dry zones over a range of environmental and surface conditions. When modelling dry zones, recent reports have arbitrarily only considered the nucleation dry zone (Guadarrama-Cetina *et al.* 2014; Sun & Rykaczewski 2016) or the flux dry zone δ_F (Guadarrama-Cetina *et al.* 2015; Nath & Boreyko 2016) in isolation. One report did compare models of δ_N and δ_F (Boreyko *et al.* 2016), but only for a single experimental data point, which cannot yield too much insight given that the model included floating parameters. Thus, which physical mechanism wins the duel of the dry zones, and when, remains completely unknown.

Here, we obtain steady-state dry zones around ice droplets and reveal the underlying physics by comparing all results to refined models of nucleation and flux dry zones. Our ability to obtain stable dry zones was enabled by the unique choice of ice as the hygroscopic material (Boreyko *et al.* 2016), whose saturation vapour pressure remains constant as it harvests water vapour and is therefore always lower than that of liquid water at the same temperature (Murphy & Koop 2005). This concept is depicted in figure 1(*a*), where a frozen droplet created an annular dry zone of length

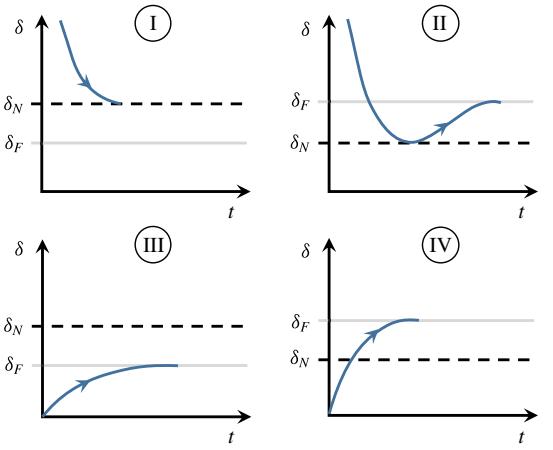

FIGURE 2. Four different possible pathways for attaining a dry zone over time. The length scale δ is the edge-to-edge distance between the hygroscopic droplet and the closest liquid droplets.

$\delta_{Cr} = 507 \pm 2$ μm between itself and forming condensation. This dry region is remarkable when considering that the surface temperature was chilled a full 16 °C beneath the dew point. The steady-state length of the annular dry zone, δ_{Cr}, that formed between the ice droplet and the condensate was measured over a variety of conditions. Refined models of both the nucleation dry zone and flux dry zone (figure 1*b*) were then developed and compared to experiments to determine which mechanism wins the duel of the dry zones.

2. Pathway dependence

A nuance not discussed in previous works is the path dependency of dry zone formation, as shown in figure 2. There are two ways to create a dry zone: by evaporating out pre-existing surrounding condensate or by growing in the condensation toward the hygroscopic droplet. Hypothetically, there are also dual scenarios of $\delta_N > \delta_F$ versus $\delta_F > \delta_N$, resulting in four total types of pathways for attaining δ_{Cr}.

When condensation is grown in toward a hygroscopic droplet for the first time, droplets are nucleating on a previously dry region. Therefore, δ would first reach δ_N and would stop there if $\delta_N > \delta_F$, because the nucleated droplets are free to grow (case I). However, if $\delta_N < \delta_F$, then the droplets in the region between δ_F and δ_N would subsequently evaporate and thus the emergent dry zone would be δ_F (case II). In § 3.2, we will describe how a humidity chamber was used to freeze a deposited water droplet in a sufficiently dry environment, in order to suppress any transient condensation effects while also evaporating any recalescence-induced condensate halos (Jung, Tiwari & Poulikakos 2012). By then increasing c_∞ (or decreasing T_w) to allow condensate to form for the first time, the steady-state dry zone can correspond to either the nucleation dry zone (case I) or the flux dry zone (case II), whichever is larger.

In contrast, when condensate has already nucleated prior to the steady-state test conditions, evaporating these droplets to create a flux dry zone is the only option. This is true regardless of whether δ_N (case III) or δ_F (case IV) is larger. A common real-life example is condensation frosting, where a surface is already populated with supercooled liquid droplets prior to the initial freezing events that induce dry zones

(Boreyko *et al.* 2016). In § 3.3, we will describe how we perform a second set of experiments in an ambient environment that exclusively promote case III or case IV dry zone formation. This approach facilitates the isolated characterization of flux dry zones, removing any possible confusion about which type of dry zone is being manifested.

3. Materials and methods

3.1. *Sample fabrication*

A silicon wafer with 100 nm of SiO_2 was cleaned with oxygen plasma for 4 min at 150 W (Plasma Etch, PE-25). Silane deposition was performed by placing the silicon wafer inside of a Pyrex pan with 20 µl of trichloro(1H, 1H, 2H, 2H-perfluorooctyl) (Sigma Aldrich). The pan was subsequently heated on a hot plate at 70 °C for 2 h to facilitate the vapour-phase deposition of a self-assembled silane monolayer on the silicon sample. The advancing and receding contact angles were measured to be $\theta_A/\theta_R = 94°/77°$ using the shrink/swell method on a contact angle goniometer (ramé-hart, Model 590), with a standard deviation of $\pm 1°$ for each angle.

3.2. *Humidity chamber experimental set-up*

For the experimental data shown in figure 3(*a*,*b*), the hydrophobic silicon chip was bonded with thermal paste to a Peltier stage inside a customized humidity chamber (ramé-hart) that was bolted underneath a top-down optical microscope (Nikon LV150). A quartz window was embedded in the chamber's roof to facilitate sample imaging with a 5, 10 or 20× objective featuring an extra-long working-distance lens (Mitutoyo). The vertical gap between the sample and the bottom of the quartz window was 2.2 cm to avoid disruption of the diffusive boundary layer that resulted during condensation. The saturation vapour pressures of water (P_w) and ice (P_i) droplets are both direct functions of temperature (Murphy & Koop 2005) and can therefore be varied in tandem (not independently) by tuning the temperature of the Peltier stage (T_w). The humidity chamber uses a hygrometer probe to measure both the air temperature (T_∞) and the relative humidity (H). Dry air is provided from an air pump connected to a tube full of desiccant, while wet air is provided by an ultrasonic humidifier. A controller determines the ratio of dry to wet air flowing into the chamber, such that relative humidity can be set to any desired value. The partial pressure of water vapour in the ambient, calculated as $P_\infty = P_w(T_\infty)H$, was controlled by varying H within the chamber.

The ambient humidity was set to a pre-determined amount, such that the initial substrate temperature was just above the critical temperature where nucleation occurs. For example, for a humidity of $H = 21\,\%$ and air temperature of $T_\infty = 21\,°\mathrm{C}$, the Peltier stage was set to $T_w = -2\,°\mathrm{C}$. Note that while $T_w = -2\,°\mathrm{C}$ actually corresponds to the dew point, nucleation did not occur because the energy barrier inherent to embryo formation requires supersaturated conditions, as will be discussed in more detail below. When the surface was completely dry, the chamber was briefly opened to deposit a $V = 10$ µl droplet of distilled water. The surface was then brought down to $-20\,°\mathrm{C}$ in order to freeze the deposited droplet. If condensation ensued during or after the freezing of the droplet, the surface temperature was either brought above the dew point (but still below 0 °C) or the humidity in the chamber was further decreased to ensure evaporation of the condensate.

Once the surface around the frozen droplet was completely dry, the Peltier stage and ambient humidity were set to their desired values to generate supercooled

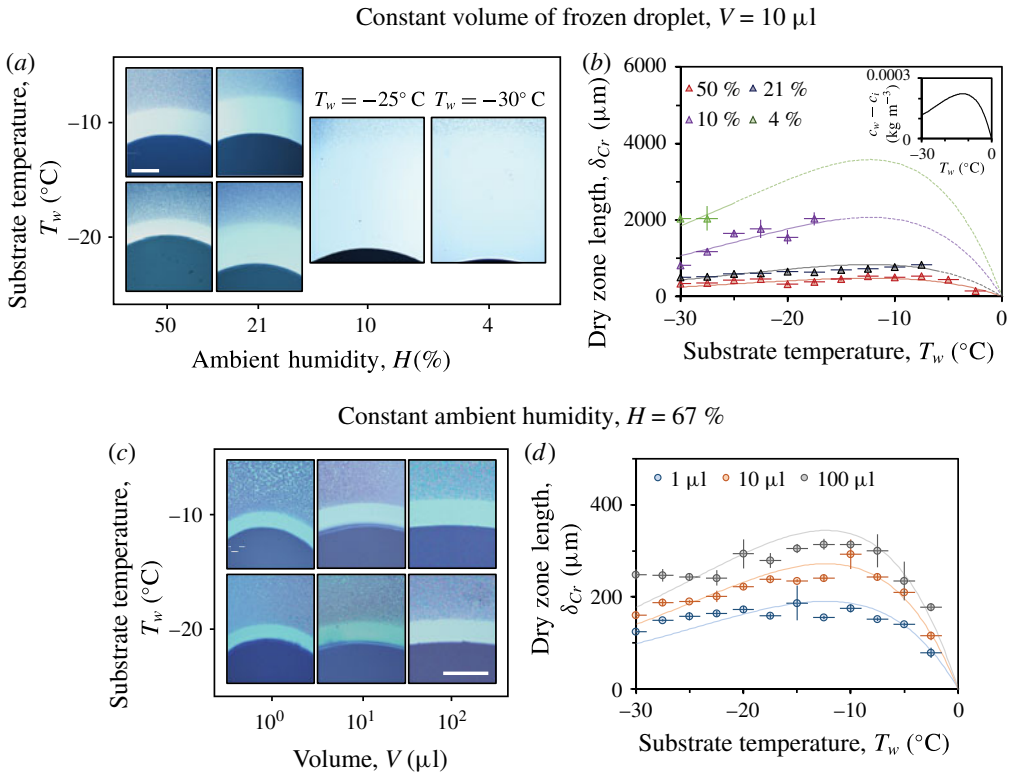

FIGURE 3. (*a*) Images and (*b*) measurements of the steady-state dry zone length (δ_{Cr}) about an ice droplet of fixed volume 10 µl for different humidities. When plotted against the substrate temperature (T_w), the δ_{Cr} curves for different humidities qualitatively trace out the variation in $(c_w - c_i)$ (inset). Note that there are no data points for the 4 %, 10 % and 21 % humidities above a critical temperature corresponding to the nucleation threshold. (*c*,*d*) Ambient experiments where the humidity was fixed, but the size of the frozen droplet was varied. The curved lines in (*b*) and (*d*) are obtained from the flux dry zone equation (5.8) developed in § 5. Horizontal error bars account for ±1 °C experimental fluctuations about the set point temperature T_w, while vertical errors bars represent plus/minus a standard deviation from the average value of δ_{Cr} measured over 3 separate trials for each chamber condition.

condensation with a steady-state dry zone about the perimeter of the ice droplet (figure 1*a*). Specifically, the surface temperature was varied from $T_w = -30\,°\mathrm{C}$ to $-2.5\,°\mathrm{C}$ while the humidity ranged from $H = 4\,\%$ to 50 %. The moment at which the set point values of surface temperature and humidity are attained corresponds to the beginning of the actual experiment itself (i.e. $t = 0$). A dry zone was considered to be in its steady-state configuration when its length remained constant under the microscope for at least 10 s. This steady-state value remained stable as long as the supercooled condensation growing beyond the dry zone remained unfrozen, which ranged from seconds to hours depending on the value of T_w. The value of δ_{Cr} was obtained by measuring the length of the dry zone at the top, bottom, left and right sides of the ice droplet and averaging together. For each combination of experimental conditions, three separate experimental trials were performed to obtain error bars for δ_{Cr}. As discussed in § 2, these dry zones must correspond to cases I or II as depicted

in figure 2, as the ice droplet was already frozen prior to the onset of condensation. The humidity chamber experienced minor fluctuations in H about its set point; the upper and lower bounds of H were recorded over the three trials of each condition in order to calculate the corresponding uncertainty in P_∞.

Averaged across all test values of T_w and H, the air temperature inside of the humidity chamber during steady-state conditions was $16 \pm 2\,^\circ$C, due to the chilled Peltier stage slightly cooling the air inside. To properly account for the non-isothermal conditions of the humidity chamber, the vapour pressures of the air/water/ice must be converted into vapour concentrations when modelling the diffusive flux of the system. Specifically, $c = P/\bar{R}T$, where $\bar{R} = 461.5$ J (kg K)$^{-1}$ is the gas constant of water vapour and P and T are the relevant pressures and temperatures: $P_w(T_w)$ and T_w for calculating the saturated vapour concentration of water (c_w), $P_i(T_w)$ and T_w for calculating the saturated vapour concentration of ice (c_i), and $P_\infty = P_w(T_\infty)H$ and T_∞ for calculating the ambient vapour concentration (c_∞).

3.3. *Ambient environment experimental set-up*

For the experiments corresponding to figure 3(*c*,*d*), a distilled water droplet that was either 1, 10 or 100 µl in volume was deposited on a hydrophobic silicon chip and placed in a dry freezer. Once the droplet was frozen, the silicon chip was quickly transferred to a nearby Peltier stage (Linkam, PE120) that was preset to the testing temperature and pre-positioned under the microscope stage. Using this alternate approach, it was observed that condensation initially formed very close to the ice droplet, and subsequently evaporated out to the steady-state dry zone. In other words, this technique facilitates case III or case IV dry zones, as discussed in § 2. We attribute this to the warming of the surface during the transfer to the Peltier, which reduces the pressure differential between ice and water (Murphy & Koop 2005) to minimize the extent of the initial dry zone. Now as the surface becomes chilled on the Peltier, the ice–water pressure differential increases to expand the dry zone to its steady-state value, resulting in the observed evaporation.

Unlike the humidity chamber experiments, these experiments were conducted in the ambient laboratory environment with a relative humidity of $H = 67 \pm 4\,\%$ and an air temperature of $T_\infty = 21.0 \pm 1.5\,^\circ$C. Instead of varying the humidity, the droplet volume was varied to determine the size effect of the hygroscopic ice on the magnitude of the dry zone. Because of minor evaporation effects when the droplets were in the freezer, the final volumes of the ice droplets were slightly smaller than the initial volumes of 1, 10 or 100 µl. To account for this, the average contact line radii of the frozen droplets were measured under the microscope to be 0.76 ± 0.03 mm, 1.75 ± 0.02 mm and 4.12 ± 0.08 mm respectively with a contact angle of approximately $91^\circ \pm 3^\circ$.

3.4. *Nucleation experimental set-up*

The vapour supersaturation required to nucleate liquid embryos on the hydrophobic silicon samples was determined experimentally. Using the humidity chamber to fix the humidity at $H = 10.3 \pm 0.4\,\%$ and the air temperature at $T_\infty = 15.7 \pm 0.1\,^\circ$C, the surface temperature was incrementally cooled until the nucleation and growth of condensate occurred at a critical temperature. This process was performed on three equivalently treated silicon chips, with three trials performed for each sample. The critical surface temperatures for nucleation to occur were $-18.3 \pm 1.2\,^\circ$C, $-19.4 \pm 1.4\,^\circ$C and $-17.3 \pm 0.9\,^\circ$C for the three respective surfaces. We now define the supersaturation

degree (*SSD*) as a ratio comparing the critical vapour concentration required for embryo nucleation (c_N) to the saturation concentration of water (c_w):

$$SSD = \frac{c_N - c_w}{c_w}. \tag{3.1}$$

Comparing the critical surface temperatures where nucleation occurred to the corresponding saturation temperatures revealed values of *SSD* ranging from 0.03–0.23, with the average being $SSD = 0.13 \pm 0.10$ (plus/minus a standard deviation). Using classical nucleation theory, this average *SSD* value corresponds to an effective surface wettability of $\theta_r = 33 \pm 5^\circ$ at nucleation sites (Nath & Boreyko 2016). While this is much lower than the surface's global receding contact angle for macroscopic droplets ($\theta_r = 89^\circ \pm 1^\circ$), it is well known that nucleation occurs at local defects that can exhibit significantly lower nucleation energy barriers (Lopez *et al.* 1993; Beysens 1995; Cha *et al.* 2017).

4. Experimental results

Using the humidity chamber as described in § 3.2, the steady-state value of the dry zone length (δ_{Cr}) was measured for surface temperatures ranging from $T_w = -30\,^\circ$C to $-2.5\,^\circ$C and ambient vapour concentrations ranging from $c_\infty = 5.6 \times 10^{-4}$ to 0.7×10^{-2} kg m^{-3} (figure 3*a*,*b*). The magnitude of δ_{Cr} increased by an order of magnitude with decreasing ambient humidity. This is intuitive, as reducing c_∞ makes it more difficult to overcome the nucleation energy barrier close to the ice (increasing δ_N) while simultaneously reducing the rate of vapour diffusing out-of-plane toward the substrate (increasing δ_F). For a given c_∞, the value of δ_{Cr} peaked at an intermediate temperature. This can be rationalized by considering that the difference in saturation vapour pressures between water and ice is maximal at $T_w = -12.5\,^\circ$C (Murphy & Koop 2005), which is indeed the approximate temperature where maximal values of δ_{Cr} tended to occur. However, it will be seen later on that the dry zone is governed by more parameters than solely $c_w - c_i$, which explains why the peaks in δ_{Cr} do not always fall exactly at $T_w = -12.5\,^\circ$C.

In a separate set of experiments, we varied the volume of the ice droplet from 1–100 µl and found that the dry zone increased with the size of the hygroscopic droplet (figure 3*c*,*d*). Unlike the experiments where humidity was varied, these experiments were performed without a controlled humidity chamber (methods detailed in § 3.3). Instead, the droplet was frozen in a dry freezer and then quickly transferred to a nearby Peltier stage in an ambient environment. The brief exposure of the surface to room temperature conditions before getting cooled by the Peltier ensured that condensation nucleated everywhere on the surface before a steady-state dry zone could subsequently form. This removes the possibility of a nucleation dry zone, which allows us to isolate the physics of a flux dry zone. It can be seen that the δ_{Cr} versus T_w curves in figure 3(*d*) are qualitatively quite similar to the curves obtained using the humidity chamber (figure 3*b*), where both nucleation and flux dry zones were possible. This suggests that the flux dry zone dominates the nucleation dry zone, which will now be confirmed using the following theoretical model.

5. Model

5.1. *Nucleation dry zone model*

A quasi-steady diffusion model can estimate the nucleation dry zone (δ_N). Extending radially from the surface of the frozen droplet, the concentration profile must exhibit

a hyperbolic profile to satisfy the Laplace equation (figure 1*b*):

$$c = c_\infty - (c_\infty - c_i)\frac{R}{r}, \tag{5.1}$$

where r is the radial coordinate and the boundary conditions are $c = c_i$ at the surface of the frozen droplet ($r = R$) and $c = c_\infty$ in the ambient ($r \to \infty$). Let c_N represent the critical vapour concentration required to nucleate a new embryo, such that $(r - R) = \delta_N$ when $c = c_N$. Using the definition of the supersaturation degree from (3.1), we can now rewrite the above equation as

$$\delta_N = \frac{R((SSD + 1)c_w - c_i)}{(c_\infty - (SSD + 1)c_w)}. \tag{5.2}$$

Noting that the saturation concentrations c_w and c_i are purely functions of the surface temperature, we see that δ_N is a function of four variables: R, c_∞, T_w and SSD. From a separate set of nucleation experiments (§ 3.4), we determined that our surface exhibited a supersaturation degree of $SSD = 0.13 \pm 0.10$; this uncertainty in SSD is the dominant source of uncertainty when calculating δ_N from (5.2).

When plotting the theoretical values of δ_N against the experimentally measured values of δ_{Cr}, the model did not match quantitatively or even qualitatively (figures 4 and 5). Even when accounting for the range of values of SSD, the predicted values of δ_N simply do not correspond to the δ_{Cr} curves. This is especially true for surface temperatures beneath $-10\,^\circ\mathrm{C}$ and/or for moderate relative humidities, where δ_N underestimates δ_{Cr} by approximately an order of magnitude. We therefore hypothesize that the flux dry zone is dominant over the nucleation dry zone, at least when using ice as the hygroscopic agent. To test this hypothesis, we must now develop a theory for the flux dry zone.

5.2. *Flux dry zone: scaling model*

For liquid droplets at the periphery of a flux dry zone, the in-plane evaporative flux (J_e) and out-of-plane condensation flux (J_c) must balance (figure 1*b*). The supercooled liquid condensate visible along the periphery of the dry zone is typically of radius $a \sim 1$–10 μm, which is one hundred times smaller than the frozen droplet radius $R \sim 1$ mm. As the liquid droplets defining the dry zone are micrometric, their Laplace pressure is small enough to approximate their vapour pressure as saturated (Nath & Boreyko 2016). We can then estimate the evaporative flux as

$$J_e \sim D\frac{c_w - c_i}{\delta}, \tag{5.3}$$

where D is the diffusivity of water vapour in air, c_w and c_i are the saturated vapour concentrations of water and ice and δ is the edge-to-edge separation between a water droplet and an ice droplet. Regarding the condensation flux, Guadarrama-Cetina *et al.* (2015) proposed that

$$J_c \sim D\frac{c_\infty - c_w}{\zeta}, \tag{5.4}$$

where c_∞ is the ambient vapour concentration and ζ is the vapour concentration boundary layer as depicted in figure 1(*b*) (Guadarrama-Cetina *et al.* 2015). Equation (5.4) assumes that the concentration profile above a population of

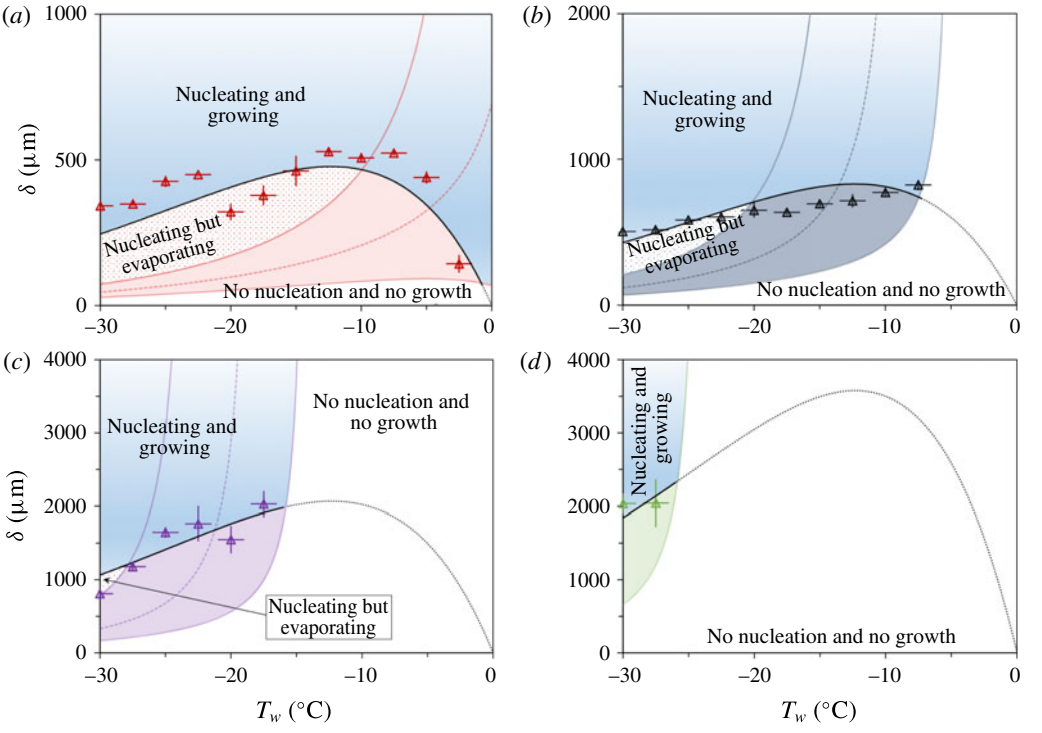

FIGURE 4. A more detailed analysis of the humidity chamber experiments from figure 3(*b*). The (*a*) red, (*b*) dark blue, (*c*) purple and (*d*) green dotted lines represent theoretical values of the nucleation dry zone (5.2) around frozen droplets of a fixed volume of $V = 10$ µl but different humidities $H = 50\,\%$, $21\,\%$, $10\,\%$ and $4 \pm 1\,\%$ respectively. The upper/lower bounds of (5.2) are denoted by solid lines and conservatively account for the maximum/minimum possible values of *SSD*. The black solid lines denote the flux dry zone (5.8). The experimental data points follow the flux lines and are finally terminated by the lower bound of the nucleation dry zones as c_∞ approaches c_N. The error bars extending from the experimental data points are identical to those defined in figure 3.

micrometric condensates is linear (Medici *et al.* 2014), as pictured in the far left of figure 1(*b*). The droplet pattern in such a case can be approximated as a homogeneous water film with an effective thickness h, with an out-of-plane concentration profile following $c = c_w + (c_\infty - c_w)(z - h)/\zeta$.

The net mass per unit time of the vapour condensing onto a liquid droplet is $\dot{m} \sim (J_c - J_e)a^2$. After normalizing the mass flow rate by its evaporative component, $\dot{M}^* = \dot{m}/J_e a^2$, a dimensionless mass flow rate is obtained:

$$\dot{M}^* \sim \frac{\delta(c_\infty - c_w)}{\zeta(c_w - c_i)} - 1. \tag{5.5}$$

By setting $\dot{M}^* = 0$, the critical distance between water and ice droplets where the flux is balanced is obtained as

$$\delta_F \sim \frac{\zeta(c_w - c_i)}{(c_\infty - c_w)}. \tag{5.6}$$

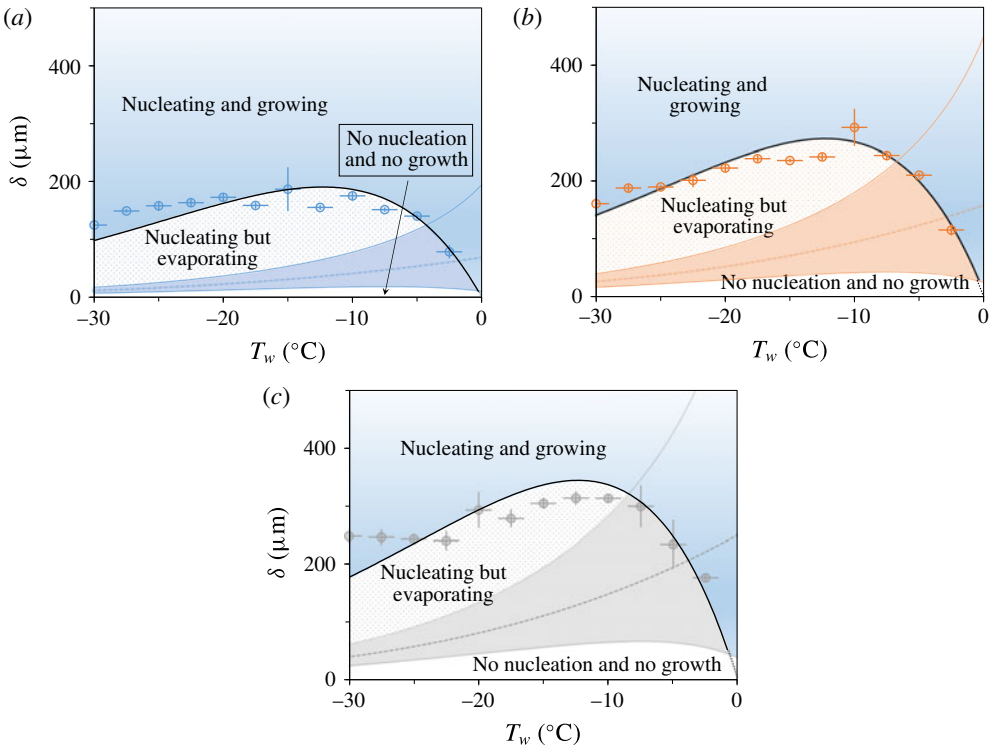

FIGURE 5. A more detailed analysis of the ambient experiments from figure 3(*d*). The (*a*) blue, (*b*) orange and (*c*) grey dotted lines denote the nucleation dry zone (5.2) around frozen droplets of volume 1, 10 and 100 µl, respectively. The fixed ambient conditions are $H = 67 \pm 4\,\%$ and $T_\infty = 21.0 \pm 1.5\,^\circ\mathrm{C}$. The two bounds of the nucleation dry zone are estimated by taking into account the variations in *SSD* and c_∞. The black solid lines denote the flux dry zone given by (5.8).

To solve for δ_F first requires a solution for the concentration boundary layer (ζ). For a purely diffusive system with negligible convective effects, ζ can be estimated from a scaling analysis of the natural convection above the cold plate for an assumed parabolic flow profile (Medici *et al.* 2014):

$$\zeta \sim \left[\frac{D\zeta_h^{3/2}}{4\sqrt{\alpha g(T_\infty - T_w)}}\right]^{1/3}, \tag{5.7}$$

where $\zeta_h \sim L_s(\alpha g(T_\infty - T_w)L_s^3/\nu^2)^{-1/5}$ is the hydrodynamic boundary layer thickness caused by buoyancy effects, α and ν are the volumetric thermal expansion coefficient and kinematic viscosity of air and L_s is the characteristic length scale of the condensing surface. For our experiments, $D \approx 2.5 \times 10^{-5}$ m^2 s^{-1} and $L_s \approx 8$ cm, such that $\zeta \sim 1$ mm over the entire range of $(T_\infty - T_w)$. More specifically, the height of the boundary layer calculated from (5.7) ranged from $\zeta \approx 1.8$–2.4 mm.

Plotting (5.6) against our experimental values of δ_F obtained mixed results (figure 6*a*). For smaller values of $(c_w - c_i)/(c_\infty - c_w)$, there was indeed a linear trend with δ_F as predicted by (5.6). However, the value of $\zeta = 1.3$ cm that captured the linear trend is an order of magnitude higher than that expected from (5.7).

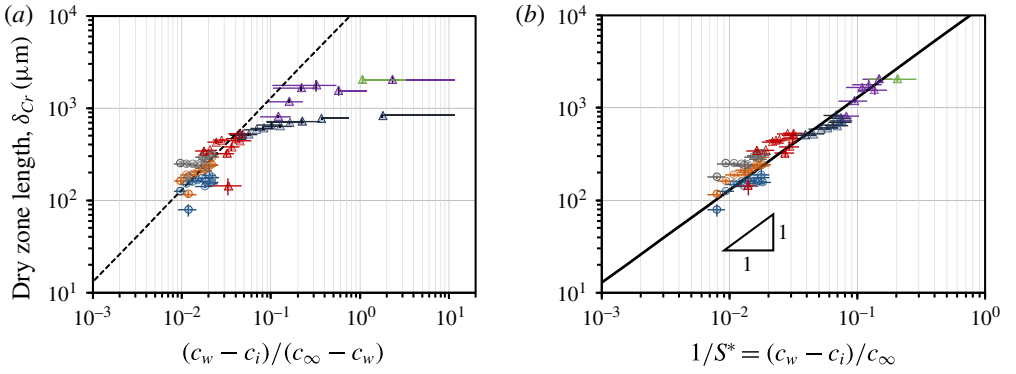

FIGURE 6. Dry zone scaling laws compared to the experimental results from figure 3(*b*) (triangles) and figure 3(*d*) (circles). (*a*) When dry zone lengths are plotted against $(c_w - c_i)/(c_\infty - c_w)$, corresponding to the original model for flux dry zones (5.6) (Guadarrama-Cetina *et al.* 2015), they increasingly move away from the power law slope of 1 at higher values. (*b*) When instead plotting against $(c_w - c_i)/c_\infty$, which corresponds to our new model for flux dry zones (5.8), all of the data collapse onto a single curve with a slope of 1. Horizontal error bars correspond to a standard deviation in c_∞ across three trials due to experimental fluctuations in relative humidity about the set point, while vertical error bars are described in figure 3.

Further, the experimental δ_{Cr} values increasingly moved away from the linear regime as $(c_w - c_i)/(c_\infty - c_w)$ was increased by 3 orders of magnitude and c_∞ approached c_w. These discrepancies suggest that the scaling model developed by Guadarrama-Cetina *et al.* (2015) may not be universally true.

The root of the conundrum can be realized by revisiting the stipulations of (5.6). First, the assumption of a constant ζ holds only if droplets on the substrate are much smaller than ζ. The radius of our frozen droplet scales with the boundary layer above the micrometric droplets, $R \sim \zeta \sim 1$ mm, and therefore would locally extend the boundary layer over its interface. Second, the assumption of a linear concentration profile only holds in the limit of $\delta \gg R$, that is, far from the frozen droplet. However, experimentally observed dry zone lengths exhibit $\delta_{Cr} \lesssim R$ (figure 3), undermining the ability to assume a linear out-of-plane concentration profile.

We now abandon the linearity assumption and instead conserve the mass flux condensing onto the substrate to the mass flux at infinity: $J_c \sim J_\infty \sim c_\infty U$, where U is the velocity of the ambient vapour far from the substrate. This in combination with (5.5) for $\dot{M}^* = 0$ yields a new scaling for the flux dry zone:

$$\delta_F \sim \frac{\zeta (c_w - c_i)}{c_\infty}, \tag{5.8}$$

where $\zeta \sim D/U$ is a diffusive length scale representing the concentration boundary layer. Equation (5.8) is plotted against all data in figure 6(*b*), with excellent agreement when using a constant $\zeta = 1.3$ cm as a fitting factor. This collapse of all data onto a universal curve validates (5.8) over (5.6) as the emergent scaling law for flux dry zones around humidity sinks.

In figure 3, the value of ζ used in (5.8) to generate the δ_F curves was slightly changed for each data series to obtain the best possible fit. Specifically, in figure 3(*b*),

$\zeta = 0.9$ cm, 1.3 cm, 1.1 cm, and 1.5 cm for $H = 4\,\%$, $10\,\%$, $21\,\%$ and $50\,\%$, respectively. In figure 3(*d*), $\zeta = 1.05$ cm, 1.5 cm and 1.9 cm for ice droplet volumes of $V = 1$ µl, 10 µl and 100 µl. The trend for ζ to slightly increase with increasing V is intuitive, as the concentration boundary layer has to wrap around the elevated surface of the ice droplet. This secondary effect of V on the value of ζ cannot be captured directly by (5.8), beyond fitting the value of ζ to the experimental data for a given ice droplet. However, two important points should be made here. First, the differences in ζ are quite modest: averaging all 7 values of ζ results in $\zeta = 1.3 \pm 0.3$ cm. This is a remarkably low standard deviation when considering that c_∞ and V were both varied experimentally by 2 orders of magnitude, so the general scaling of $\zeta \sim 1$ cm is quite robust. This explains why all of the data could collapse in figure 6(*b*) using only the averaged value of $\zeta = 1.3$ cm. Second, when desired, numerical methods can more directly account for the size effects of the frozen droplet on the boundary layer, as will be seen in § 5.3.

The concentration boundary layer ζ can be related to the Péclet number to compare advective versus diffusive transport, as shown in (Nishinaga 2014, pp. 669–695):

$$Pe = \frac{RU}{D} = \frac{R}{\zeta}. \tag{5.9}$$

The value of $\zeta = 1.3$ cm that was used to fit (5.8) to the experimental data in figure 6(*b*) results in $Pe \approx 0.08 < 1$ for $R \sim 1$ mm, confirming that U is a purely diffusive velocity. This fitted value of ζ can be physically rationalized by considering the hyperbolic concentration profile about the isolated frozen droplet (5.1). Rescaling the variables as $c^* = (c - c_i)/(c_\infty - c_i)$ and $r^* = r/R$, we get $\nabla^2 c^* = 0$. With the boundary conditions $c^*(r^* = 1) = 0$ and $c^*(r^* \to \infty) \to 1$, we obtain the solution of $c^* = 1 - 1/r^*$. Of course, the hyperbolic profile will never fully attain $c^* = 1$, but an effective boundary layer could be approximated as $c^* \approx 0.9$. When plugging in $r = \zeta = 1.3$ cm about a millimetric frozen droplet ($R = 1$ mm), a concentration of $c^* \approx 0.923$ is obtained. This confirms that the fitted value of ζ is a reasonable physical representation of the height of the concentration boundary layer. A typical velocity of vapour diffusing toward the substrate therefore scales as $U \sim D/\zeta \sim 1$ mm s^{-1}, when using $D \approx 2.5 \times 10^{-5}$ m^2 s^{-1}. While the exact magnitude of U can change with the system conditions, we expect that the scaling of $U \sim 1$ mm s^{-1} is broadly true for a purely diffusive system given that the aforementioned variations in ζ were quite minor even with major variations in c_∞, T_w and V.

Finally, we introduce a dimensionless supersaturation parameter that compares the ambient concentration to the differential between water and ice

$$S^* \sim \frac{c_\infty}{c_w - c_i}, \tag{5.10}$$

which allows (5.8) to be succinctly expressed as

$$\delta_F \sim RPe^{-1}S^{*-1}. \tag{5.11}$$

In the present context of freezing a deposited droplet, the maximum liquid height is $h = 2l_c \sin(\theta/2)$ for puddles where $l_c \sim \sqrt{\sigma/\rho g}$ is the capillary length (Quere 2005). Therefore an upper bound for the dry zone length should scale as $\delta_{Cr,max} \sim l_c Pe^{-1}S^{*-1}$ when $\theta \approx 90°$.

5.3. *Flux dry zone: numerical model*

The scaling law governing the flux dry zone (5.8) is corroborated by simulations that solved the diffusion equation to explicitly obtain the flux dry zone length. The steady-state concentration field is governed by the Laplace equation, $\nabla^2 c = 0$, where c is the water vapour concentration. To make the problem tractable, the condensed water droplets were approximated as a thin water film on the substrate while the ice droplet was assumed hemispherical. Thus the problem is axisymmetric and can be solved in a two-dimensional computational domain. We imposed Dirichlet conditions $c = c_\infty$, $c = c_i$, and $c = c_w$ on the upper boundary, ice surface and the water film, respectively; the no-flux condition was imposed on the rest of the boundary. Note that the temperature field did not need to be explicitly calculated to model the diffusive transport; rather, the temperatures define the aforementioned boundary conditions for the concentration field. In order to capture the dry zone length, the inner edge of the water film was repositioned until it coincided with the stagnation point of the diffusive streamlines. By diffusive streamlines, we mean the lines that run tangential to the concentration gradient along which the vapour flows toward the substrate. We define the stagnation point as the location on the surface where the streamlines point toward the solid surface on one side but toward the hygroscopic droplet on the other side. (Considering the axisymmetric geometry, technically the stagnation 'point' is actually a line.) For each water film, the Laplace equation was solved by a finite element method using the COMSOL Multiphysics software. To ensure numerical accuracy, the computational mesh was refined in a small region above the dry zone, with the finest element size being approximately one thousandth the size of the ice radius.

Figure 7(*a*) visualizes the concentration field and resulting dry zone about a hygroscopic droplet. To aid in the reader's visualization of the streamlines, we intentionally dramatized the hygroscopicity of the 'ice' droplet by imposing a ratio of $c_i/c_w = 0.75$ and a moderate supersaturation of $c_\infty/c_w = 1.5$. In contrast, the concentration ratio for a water/ice system is a more modest $c_i/c_w = 0.91$ at $T_w = -10\,^\circ\mathrm{C}$. The non-dimensional domain height is $H/R = 5/2$, where R is the radius of the hygroscopic droplet. At a critical length from the edge of the hygroscopic droplet, the vapour concentration near the surface becomes saturated with respect to liquid water ($c/c_w = 1$), which can also be conceptualized as the stagnation point for the diffusive flow field. In other words, the liquid condensation does not exhibit a net diffusive flux at this location, effectively representing the flux dry zone δ_F. Within the dry zone itself, the concentration field is subsaturated ($c/c_w < 1$) despite the supersaturated ambient, due to the presence of the hygroscopic droplet. As a result, vapour within this dry zone gets directed toward the hygroscopic droplet, leaving the substrate itself dry. In figure 7(*b*), we magnify the dry zone region to more clearly visualize how the presence of condensation disrupts the concentration field about the hygroscopic droplet. The concentration profile about the hygroscopic droplet is initially hyperbolic, but becomes influenced by the nearby liquid condensate midway into the dry zone. Changing perspectives, it is also apparent that the presence of the hygroscopic droplet alters the concentration profile above the liquid film. Close to the dry zone, the concentration profile above the condensate is neither linear nor varying purely in the out-of-plane direction. This helps explain why the classical scaling for the diffusive growth of condensate (5.4) was not completely successful in modelling the flux dry zone in the presence of a hygroscopic droplet, requiring our new scaling represented by (5.8).

To make direct comparisons to the experimental results and scaling analysis, this computational analysis was performed for physical values of the concentration

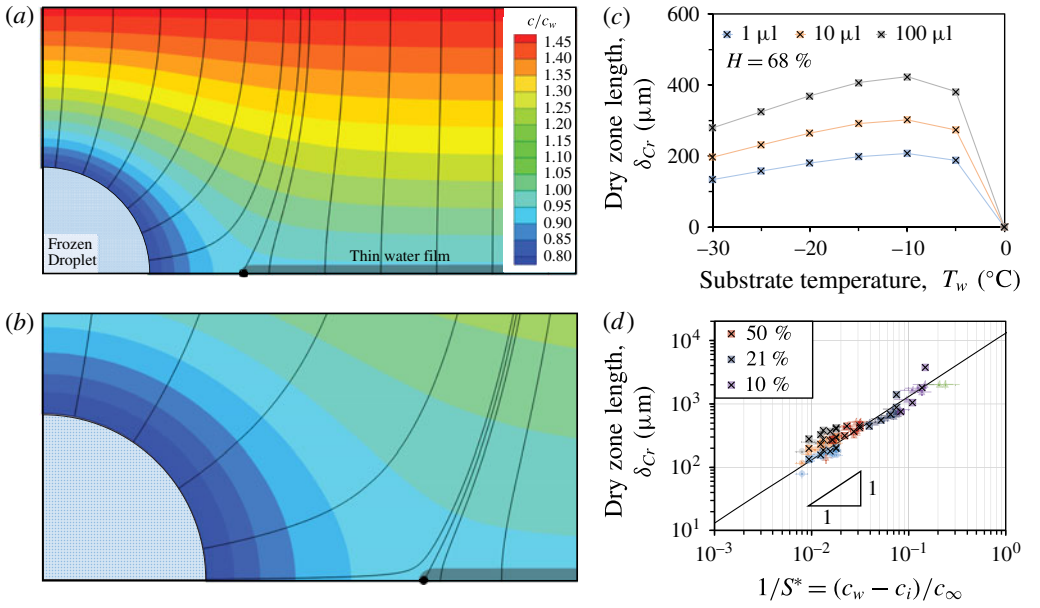

FIGURE 7. (*a*) Simulated concentration field around a hygroscopic droplet. The supercooled liquid condensate was approximated as an infinitesimally thin water film (drawn as a dark grey line to the right of the hygroscopic droplet). The black curves correspond to the diffusive streamlines of the water vapour in the air. The colour map quantifies the value of c/c_w throughout the concentration field, where an artificially large hygroscopicity of $c/c_w = 0.75$ was imposed at the interface of the 'ice' droplet to aid in the visualization of the streamlines. (*b*) Zoomed-in version of (*a*), where it can be seen that vapour within the dry zone flows toward the hygroscopic droplet, while stagnating at the leading edge of the condensation (black dot). (*c*) Numerical results of dry zones around frozen droplets of 1, 10 and 100 µl corresponding to ambient conditions equivalent to the experiments in figure 3(*d*). (*d*) Numerically obtained δ_{Cr} for three different humidities (square data points with 'x' fill) are directly compared to their experimental analogues (circles and triangles), with all data collapsing onto the scaling law (5.8).

boundary conditions. In other words, the proper value of c_i/c_w was determined for each desired surface temperature using the saturation curves (Murphy & Koop 2005), while the value of c_∞/c_w was additionally dependent upon the desired temperature and humidity of the ambient air. A dimensional computational domain of 10 mm × 5 mm was used, with the size of the ice droplet corresponding to a hemi-spherical droplet volume of $V = 1$ µl, 10 µl or 100 µl. The surface temperature was varied from $T_w = -30\,^\circ\mathrm{C}$ to $-5\,^\circ\mathrm{C}$, mimicking the same general temperature range that was tested experimentally. Figure 7(*c*) graphs how the numerically derived values of δ_{Cr} vary with T_w and V for a fixed c_∞. When comparing to the experimental curves in figure 3(*d*), it can be seen that there is an excellent match qualitatively. Quantitatively, the simulated and experimental values of δ_{Cr} are of the same order of magnitude across the entire parameter space, with particularly good agreement at colder temperatures. Unlike the scaling analysis, the simulation was able to directly capture the effect of increasing δ_{Cr} with increasing V, without requiring a floating parameter. Also, note the $\delta - T_w$ curves closely follow the variation of $(c_w - c_i)$ with

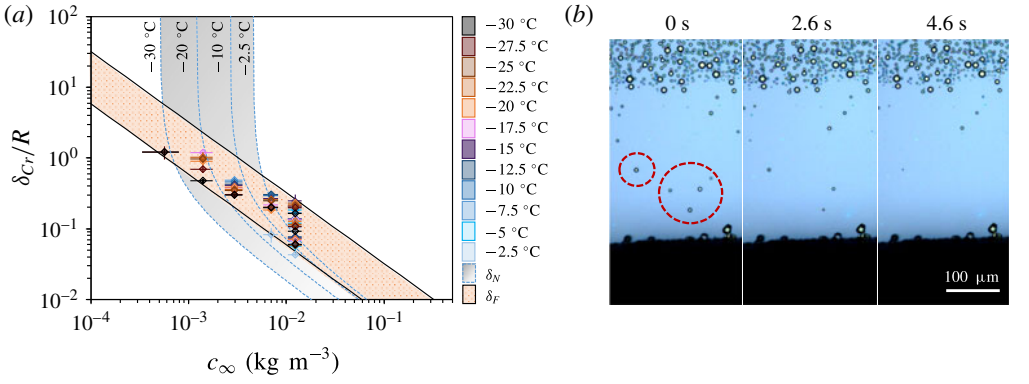

FIGURE 8. (*a*) Phase map summarizing the duel of the nucleation and flux dry zones. Dry zone lengths are non-dimensionalized with the radius of the frozen droplet and plotted against the ambient vapour concentration. The grey and orange regions correspond to the theoretical values of nucleation dry zones (δ_N^*, equation (5.2)) and flux dry zones (δ_F^*, equation (5.8)), respectively. A constant value of $SSD \approx 0.128$ for all temperatures was used to calculate δ_N^*, as indicated by our experimental observations. The upper and lower bounds of the orange band correspond to the minimum and maximum values of $c_w - c_i$ from our experiments, which were obtained at temperatures of $T_w = -12.5\,^\circ\mathrm{C}$ and $-30\,^\circ\mathrm{C}$, respectively. The experimental data points, collected from figure 3(*b*,*d*) and colour coded by the substrate temperature, universally fall within the orange region to suggest that the flux dry zone is always dominant ($\delta_{Cr}^* \sim \delta_F^*$). (*b*) When rain droplets fell within the dry zone (first panel, outlined in red), they completely evaporated within seconds (second and third panels) while the droplets at the periphery of the dry zone remained unchanged in size. See Movie 1 in the supplementary material (available at https://doi.org/10.1017/jfm.2018.579).

temperature (see inset of figure 3*b*). Finally, in figure 7(*d*), the numerically simulated values of δ_{Cr} are directly compared with the experimental data as a function of both T_w and c_∞. All of the data, both computational and experimental, obey the universal scaling law given by (5.8). The numerical data points represent a fixed ice droplet volume of $V = 10$ µl, and for the $H = 21\,\%$ simulations the lower-bound estimate of the experimental c_∞ was used in addition to the averaged value, in order to show that the scaling law holds even when accounting for humidity fluctuations in the chamber. The experimental data points represent all of the measurements shown in figure 3(*b*) (triangles) and figure 3(*d*) (circles).

5.4. *Phase map*

A phase map is constructed in figure 8(*a*) to directly compare nucleation dry zones (5.2) and flux dry zones (5.8). When superimposing our experimental data from figure 3 onto the phase map, we find that $\delta_N > \delta_F$ is only possible when the substrate is extremely close to the dew point. In other words, as $c_\infty \to c_N$, the nucleation dry zone shoots up asymptotically toward infinity and $\delta_N > \delta_F$ is true. The phase map shows that all of our experimental dry zone lengths fall in the orange region corresponding to flux dry zones: $\delta_F > \delta_N$. Obtaining data points in the asymptotic region of δ_N would require exceptional control over the ambient humidity and substrate temperature, as even a slight variation may cause it to return to the flux curve or go above the dew point. Our experimental set-up was not sensitive enough

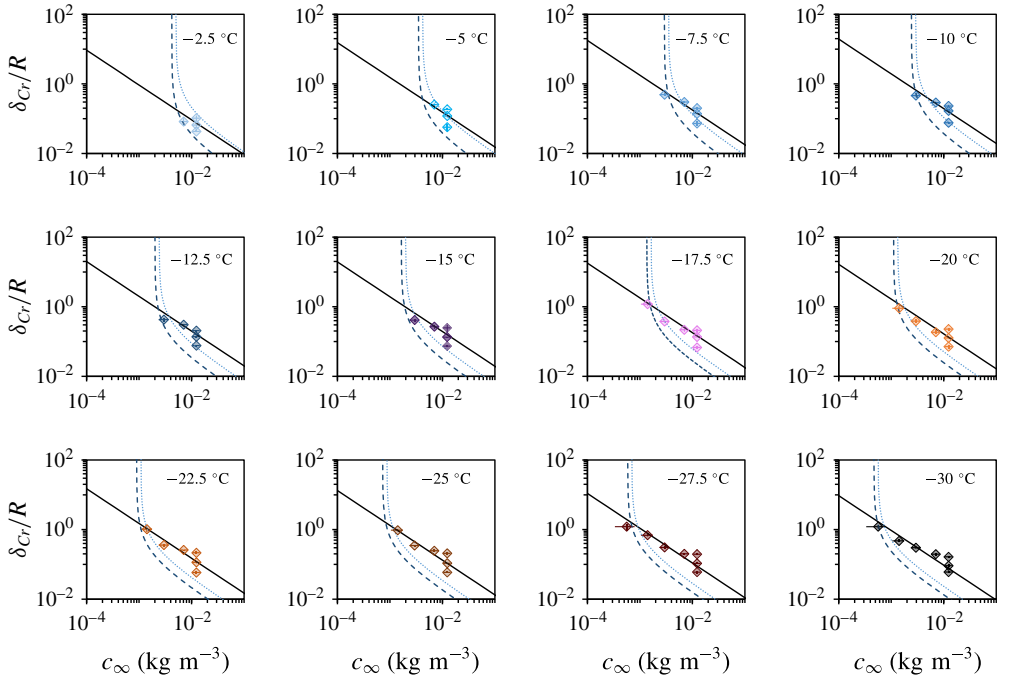

FIGURE 9. Phase map of nucleation and flux dry zones at different surface temperatures, $-30 \leqslant T_w < 0\,^{\circ}\mathrm{C}$, at 2.5 °C intervals. The dashed lines correspond to the dimensionless nucleation dry zone, δ_N^*, at a fixed temperature (dark blue for $SSD = 0.03$, light blue for $SSD = 0.23$). The solid line corresponds to the dimensionless flux dry zone, δ_F^*, at constant temperature. Note that δ_{Cr}, which corresponds to the greater of the two dry zones, demarcates the condensing versus dry regions.

for such an investigation. Nevertheless, our experimental findings and theoretical estimates provide conclusive evidence that the critical dry zone around a frozen droplet practically always corresponds to the flux dry zone, $\delta_{Cr} \sim \delta_F$. This explains why the experimental curves in both figures 3(*b*) and 3(*d*) are qualitatively similar and all agree with (5.8), despite the fact that both nucleation and flux dry zones were hypothetically possible in the former (case I and II pathways, refer to figure 2) while only flux dry zones were possible for the latter (case III and IV pathways). In figure 9, a separate phase map is created for each value of T_w to simplify the calculations of δ_N and δ_F and aid the visual comparison to the experimental data points. With this cleaner format, we were able to plot the upper and lower bounds for δ_N due to the uncertainty in *SSD*, as opposed to figure 8(*a*) which only plots the average theoretical value of δ_N for each given temperature.

As a final confirmation that δ_{Cr} is a flux dry zone, we observed that micrometric rain droplets were able to spontaneously form and gently fall onto the dry zone when the air was warm and humid ($H = 65.4\,\%$, $T_\infty = 23.8\,^{\circ}\mathrm{C}$) and the surface was sufficiently cold ($T_w = -30\,^{\circ}\mathrm{C}$). Every microdroplet landing within the dry zone promptly evaporated within a few seconds, regardless of which region of the dry zone it landed in, which provides direct experimental confirmation that the entire dry zone is a region of inhibited growth (figure 8*b*).

A subtle question remains unanswered: how were the freshly nucleated nanodroplets able to initially grow into the flux-balanced microdroplets comprising the periphery

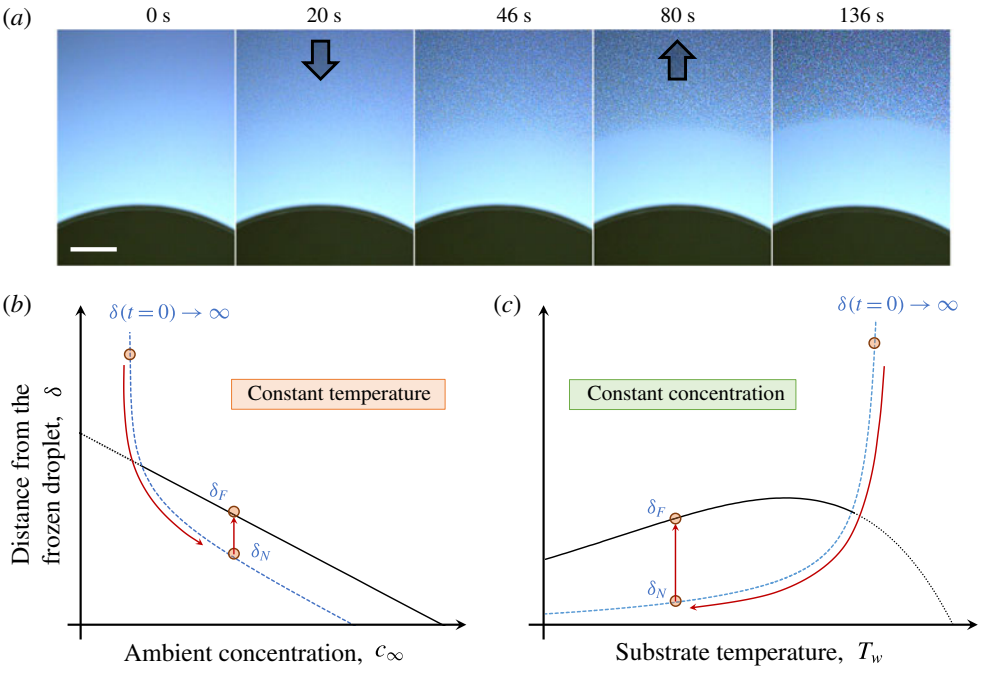

FIGURE 10. (*a*) Condensation grows radially inward toward the frozen droplet and then subsequently evaporates out to settle at the flux dry zone. The steady-state dry zone in the figure corresponds to a frozen droplet of volume $V = 10$ µl at a substrate temperature $T_w = -12.5\,^{\circ}\mathrm{C}$, air temperature $T_\infty = 14.9\,^{\circ}\mathrm{C}$ and humidity of $H = 21\,\%$. Scale bar denotes 100 µm. (*b*) Schematic of how δ evolves over time when the substrate temperature is kept constant and c_∞ is gradually increased. (*c*) Schematic of how δ evolves over time when c_∞ is held constant and T_w is decreased from the dew point to the desired value. See Movie 2 in the supplementary material.

of the dry zone? This seems paradoxical, as the appreciable Laplace pressure of nanodroplets renders them highly supersaturated and therefore more susceptible to evaporation compared to the microdroplets. The answer is found by recalling that the nucleation dry zone is always smaller than the flux dry zone ($\delta_N < \delta_F$). When droplets first nucleate on the surface, the dry zone is initially smaller (δ_N), but then expands as these nucleated droplets evaporate (case II in figure 2). This would result in the 'breathing' of the dry zone, which is indeed what we observe here (figure 10*a*). During this breathing event, the nucleated nanodroplets have to disappear one row at a time, as the ice predominantly interacts with its nearest liquid neighbours. In other words, the rows of droplets behind the front row are free to continue growing, as the water in the front is shielding these droplets from the hygroscopic ice. By the time the ice droplet is interacting with the row of droplets corresponding to the periphery of the flux dry zone, they have conveniently already grown into micrometric (i.e. saturated) droplets visible under a microscope. This explains how the droplets at the periphery of the dry zone were able to grow to a microscopic size in the first place, and also explains why at least a portion of the breathing dynamics is visible under a microscope despite the fact that nucleating embryos are initially only 1–10 nm in size. The time scale of this transient process leading up to the steady-state dry zone was of order $t \sim 1$ min in most cases, and is related to the time required to reach

the desired humidity or surface temperature and simultaneously involves the time required for the droplets to nucleate in and evaporate out.

Figure 10(*b*) illustrates the pathway of a breathing dry zone under constant surface temperature conditions. The dotted blue line corresponds to the nucleation dry zone, δ_N, and the black solid line represents the flux dry zone, δ_F. As c_∞ is increased, δ initially moves along the dotted blue line until c_∞ reaches its steady-state value. This sets $\delta = \delta_N$, but δ_N being below δ_F, the nucleated droplets cannot survive and evaporate out to the distance δ_F. Finally, figure 10(*c*) represents the dynamics of a dry zone when now the ambient vapour concentration is fixed and the surface temperature is decreased. Initially δ follows the δ_N curve, but once T_w reaches steady state, the dry zone must expand to δ_F by evaporating some of the nucleated droplets. Both pathways lead to initial condensation up to δ_N and subsequent evaporation to δ_F.

6. Conclusion

In conclusion, we have obtained stable dry zones around hygroscopic ice droplets that remain free of condensation or frost even when the surface is well beneath the dew point. Across a very wide parameter space, the length of dry zones collapsed onto a universal scaling law corresponding to a region of inhibited droplet growth, which dominated the region of inhibited droplet nucleation. Therefore, regarding the duelling mechanisms of a nucleation dry zone versus a flux dry zone, we can declare the flux dry zone the emphatic victor. More specifically, the following advances were made regarding our understanding of dry zones:

(i) We generated stable dry zones by utilizing frozen water as the hygroscopic medium, as the vapour pressure of ice remains depressed even as it harvests moisture from the air. In contrast, studies using salts, glycols or nectars are limited by the transient collapse of dry zones as the hygroscopic agent becomes diluted with water over time.

(ii) We clarified the pathway dependence of dry zone formation. When a substrate already exhibits condensation prior to the freezing of a droplet into hygroscopic ice, the dry zone is formed by evaporating liquid droplets and must correspond to a flux dry zone. Conversely, when a surface already contains the hygroscopic material prior to condensation, both nucleation and flux dry zones are possible and whichever is larger will govern the dry zone's length.

(iii) A previous report assumed a linear concentration profile above the condensation when modelling the flux dry zone (5.6). Here, we showed that this linearity assumption breaks down in the presence of a hygroscopic droplet and developed a new scaling model for the flux dry zone that collapsed all of the experimental data (5.8).

(iv) The vast majority of previous reports of dry zones have posited a mechanism of inhibited droplet nucleation (Aizenberg *et al.* 1999; Guadarrama-Cetina *et al.* 2014; Medici *et al.* 2014; Biswas *et al.* 2015; Sun *et al.* 2015; Sun & Rykaczewski 2016). Our findings clearly show, over a wide variety of surface temperatures and ambient conditions, that dry zones are governed by a mechanism of inhibited droplet growth. We showed that the theoretical values for nucleation dry zones do not even match qualitatively with the experimental trends, revealing that the mechanism for dry zones is not inhibited nucleation after all.

(v) We developed a computational method for estimating the length of a flux dry zone, by imposing boundary conditions for the concentration field and locating

the stagnation point of the diffusive vapour flow field. This numerical approach agreed well with the experimental results and scaling model, and should be able to provide versatile predictions of dry zone lengths for any desired geometry and hygroscopic material.

(vi) After confirming that the dominant mechanism for the dry zones is inhibited growth, we demonstrated that microdroplets impacting the dry zone will spontaneously evaporate due to the presence of the hygroscopic droplet. This is remarkable given the large degree of supersaturation in the ambient.

We hope that our model can rationalize future work on anti-fogging and anti-frosting surfaces that utilize overlapping dry zones between hygroscopic materials such as glycols, salts or even ice itself.

Acknowledgements

The first two authors made an equal contribution to this paper. This work was supported by the National Science Foundation (CBET-1604272) and startup funds from the Department of Biomedical Engineering and Mechanics at Virginia Tech. We thank F. Ahmadi for fruitful discussions.

Supplementary movies

Supplementary movies are available at https://doi.org/10.1017/jfm.2018.579.

REFERENCES

AIZENBERG, J., BLACK, A. J. & WHITESIDES, G. M. 1999 Oriented growth of calcite controlled by self-assembled monolayers of functionalized alkanethiols supported on gold and silver. *J. Am. Chem. Soc.* **121**, 4500–4509.

BEYSENS, D. 1995 The formation of dew. *Atmos. Res.* **39**, 215–237.

BISWAS, S., CHAKRABARTI, A., CHATEAUMINOIS, A., WANDERSMAN, E., PREVOST, A. M. & CHAUDHURY, M. K. 2015 Soft lithography using nectar droplets. *Langmuir* **31**, 13155–13164.

BOREYKO, J. B., HANSEN, R. R., MURPHY, K. R., NATH, S., RETTERER, S. T. & COLLIER, C. P. 2016 Controlling condensation and frost growth with chemical micropatterns. *Sci. Rep.* **6**, 19131.

CHA, H., WU, A., KIM, M. K., SAIGUSA, K., LIU, A. & MILJKOVIC, N. 2017 Nanoscale-agglomerate-mediated heterogeneous nucleation. *Nano Lett.* **17**, 7544–7551.

CHAN, C. W., LING-CHIN, J. & ROSKILLY, A. P. 2013 A review of chemical heat pumps, thermodynamic cycles and thermal energy storage technologies for low grade heat utilisation. *Appl. Therm. Engng* **50**, 1257–1273.

CHEN, X., GOODNIGHT, D., GAO, Z., CAVUSOGLU, A. H., SABHARWAL, N., DELAY, M., DRIKS, A. & SAHIN, O. 2015 Scaling up nanoscale water-driven energy conversion into evaporation-driven engines and generators. *Nat. Commun.* **6**, 7346.

DAWSON, C., VINCENT, J. F. V. & ROCCA, A. M. 1997 How pine cones open. *Nature* **390** (6661), 668.

GUADARRAMA-CETINA, J., MONGRUEL, A., GONZALEZ-VINAS, W. & BEYSENS, D. 2015 Frost formation with salt. *Europhys. Lett.* **110**, 56002.

GUADARRAMA-CETINA, J., NARHE, R. D., BEYSENS, D. A. & GONZALEZ-VINAS, W. 2014 Droplet pattern and condensation gradient around a humidity sink. *Phys. Rev.* E **89**, 012402.

JUNG, S., TIWARI, M. K. & POULIKAKOS, D. 2012 Frost halos from supercooled water droplets. *Proc. Natl. Acad. Sci. USA* **109**, 16073–16078.

LOPEZ, G. P., BIEBUYCK, H. A., FRISBIE, C. D. & WHITESIDES, G. M. 1993 Imaging of features on surfaces by condensation figures. *Science* **260**, 647–649.

MEDICI, M. G., MONGRUEL, A., ROYON, L. & BEYSENS, D. 2014 Edge effects on water droplet condensation. *Phys. Rev.* E **90**, 062403.

MURPHY, D. M. & KOOP, T. 2005 Review of the vapour pressures of ice and supercooled water for atsmopheric applications. *Q. J. R. Meteorol. Soc.* **131**, 1539–1565.

NARAYANAN, S., LI, X., YANG, S., KIM, H., UMANS, A., MCKAY, I. S. & WANG, E. N. 2015 Thermal battery for portable climate control. *Appl. Energ.* **149**, 104–116.

NATH, S. & BOREYKO, J. B. 2016 On localized vapor pressure gradients governing condensation and frost phenomena. *Langmuir* **32**, 8350–8365.

NISHINAGA, T. 2014 *Handbook of Crystal Growth: Fundamentals*. Elsevier.

QUERE, D. 2005 Non-sticking drops. *Rep. Prog. Phys.* **68**, 2495–2532.

REYSSAT, E. & MAHADEVAN, L. 2009 Hygromorphs: from pine cones to biomimetic bilayers. *J. R. Soc. Interface* **6** (39), 951–957.

SUN, X., DAMLE, V. G., UPPAL, A., LINDER, R., CHANDRASHEKAR, S., MOHAN, A. R. & RYKACZEWSKI, K. 2015 Inhibition of condensation frosting by arrays of hygroscopic antifreeze drops. *Langmuir* **31**, 13743–13752.

SUN, X. & RYKACZEWSKI, K. 2016 Suppression of frost nucleation achieved using the nanoengineered integral humidity sink effect. *ACS Nano* **11**, 906–917.

WILLIAMS, R. & BLANC, J. 1981 Inhibition of water condensation by a soluble salt nucleus. *J. Chem. Phys.* **74** (8), 4675–4677.